

Antenna Pointing Compensation Based on Precision Optical Measurement Techniques

L. L. Schumacher and H. C. Vivian
Automated Systems Section

The pointing control loops of the DSN 70-meter antennas extend only to the Intermediate Reference Structure (IRS). Thus, distortion of the structure forward of the IRS due to unpredictable environmental loads can result in uncompensated boresight shifts which degrade blind pointing accuracy.

A system is described which can provide real-time bias commands to the pointing control system to compensate for environmental effects on blind pointing performance. The bias commands are computed in real time based on optical ranging measurements of the structure from the IRS to a number of selected points on the primary and secondary reflectors.

I. Background

The DSN 70-meter antenna pointing system derives the main Az-El pointing servo drive error signals from a two-axis autocollimator mounted on the Intermediate Reference Structure (IRS) [1]. The autocollimator projects a light beam to a precision mirror mounted on the Master Equatorial (ME) and detects elevation/cross-elevation errors (non-parallelism) between the two reference surfaces by measuring the angular displacement of the reflected beam. Thus, the pointing control loop extends only as far as the IRS, which is located aft of the main antenna structure near the intersection of the Az-El axes (see Fig. 1). Since the main antenna structure is outside the pointing control loop, distortion of the structure due to environmental loads can result in uncompensated RF boresight shift. While deformations and misalignments of the main paraboloid, subreflector, and feed cone can individually pro-

duce equivalent pointing shifts of nearly a degree due to environmental loads, self-compensating effects in the structural design of the antenna limit the net peak pointing offset to approximately 100 millidegrees.

The effect of structural distortion on pointing performance is illustrated in Fig. 2. Under design conditions, the main reflector paraboloid and subreflector hyperboloid axes lie on an axis normal to the IRS which passes through the paraboloid vertex. Environmental forces which distort the structure, as indicated by the broken line, cause rays reflected from different segments of the antenna to concentrate off the IRS reference axis. The objective of a pointing error compensation system design is to bias the pointing command so that the centroid of energy to and from the desired RF target falls along the IRS reference axis.

The following discussion presents a description and an analysis of a real-time optical measurement and processing concept which outputs real-time pointing system bias commands to compensate for the effects of environmentally induced structural distortions. The system optically measures the displacements of selected points on the main reflector and subreflector relative to the IRS. The discussion assumes that pointing of the IRS via the ME is error-free and deals only with the effects of environmentally induced distortions of the main paraboloid and displacements of the subreflector.

II. Environmental Effects

The principal environmental loads acting on the antenna are gravity, wind, and thermal effects. Gravity, the largest but most predictable load on the structure, causes sagging of the main paraboloid which varies as a function of elevation angle. Gravity also creates loads in the quadripod structure which displace the subreflector in the elevation direction. The effects of gravity are accounted for in the finite element models of the DSN antenna structures. Lookup tables constructed from finite element structural model data are currently used to provide an elevation pointing command bias signal to compensate for gravity-induced pointing error as a function of elevation angle.

Wind and thermal effects on the structure are less severe than gravity, but they are also much less predictable and can cause pointing errors in both the elevation and cross-elevation axes. These effects could also be included in the finite element structural models of the antennas, but in order to provide effective (real-time) blind pointing compensation, accurate and instantaneous knowledge of the true wind vector and thermal profile of the structures is required.

Through the use of lookup tables to bias the elevation pointing command to compensate for gravity effects, a blind pointing capability of 4 to 6 millidegrees rms is currently achievable in benign weather, with the accuracy degrading to about 12 millidegrees rms under moderately windy conditions. With the recently completed upgrades to enlarge and improve the shape of the large DSN tracking antennas in combination with future plans to quadruple the upper operating frequency, it will be necessary to improve blind pointing precision to 1 millidegree rms to fully realize the benefits of the upgrades for 32-GHz (Ka-band) operation.

III. Measurement Concept

A system of multiple point-to-point measurements using optical ranging techniques was conceived as a method for measuring and estimating the effects of structural distortions on

blind pointing accuracy in real time. It was recognized at the outset that a large number of measurement configurations are possible and that trade-offs exist between the number, location, and accuracy of measurements. To establish a baseline, a simple configuration was analyzed to determine the measurement accuracy required to meet a blind pointing accuracy of one millidegree rms. The analysis was divided into two parts: (1) a determination of the required measurement resolution; and (2) an evaluation of the effects of systematic (i.e., scale factor) errors on pointing offset determination. Also, because the main paraboloid boresight axis and subreflector positions can shift relative to each other, separate analyses of measurement resolution and systematic error requirements were made for these two major elements of the Cassegrain system. For analysis purposes, the measurement baseline was assumed to be located at the main paraboloid vertex. Since the IRS is actually located approximately 7 meters aft of the vertex, implementation of the system will require transfer of the IRS reference plane to the baseline measurement plane by optical or other methods. The main paraboloid and quadripod structures are considered to be flexible, whereas the subreflector itself is assumed to be a rigid assembly.

The SHAPES (Spatial High Accuracy Position Encoding Sensor) system under development at JPL [2] was taken as the baseline sensor for the measurement system since it is capable of multiple simultaneous high-speed (10 frames/sec) ranging measurements with accuracies at the submillimeter level. SHAPES is a time-of-flight laser ranging sensor which measures ranges from multiple sources to retroreflector targets placed at any desired (unobstructed) location throughout the structure. Each SHAPES "head" can accommodate up to 30 sources, whose actual locations can be remote from the head and optically connected through optical fibers. The measurement configuration employed for the analyses uses two-dimensional triangulation techniques to precisely determine shifts in the positions of preset targets relative to IRS coordinates due to structural distortions caused by environmental forces. From these, the "structural" boresight of the main paraboloid and the deviation of the subreflector relative to the IRS are determined by geometric calculations. These two quantities must be combined to determine the net shift of the boresight due to environmental forces. This determination is then used in computing pointing bias commands to compensate for structural distortions.

IV. Primary Reflector Structural Boresight Axis Determination

A. Measurement Configuration

The optical measurement configuration chosen as a test case for the analysis below is shown in Fig. 3. The configura-

tion was selected as one which maximizes the amount of useful boresight determination data for the number of measurements made. In this design, three SHAPES sources are placed in a precise pattern centered on the physical vertex of the main paraboloid at the base of the feed cone and aligned parallel to the elevation-bearing axis. They have unobstructed views of four retroreflectors equally spaced around the perimeter of the main dish. Two retroreflectors are placed on the antenna rim diametrically opposite each other such that the plane passing through the retros and the vertex is parallel to the elevation axis. (This is referred to as the elevation-boresight plane.) This retro placement is chosen to provide the greatest detection sensitivity to distortions caused by forces acting parallel to the surface of the Earth (i.e., crosswinds). Two other retroreflectors are located diametrically opposite each other such that the plane (e.g., the cross-elevation-boresight plane) passing through the retros and the vertex is orthogonal to the elevation axis. This set of retros provides the greatest detection sensitivity to distortions caused by gravity. The key assumption made is that the intersection of the planes containing the antenna vertex and the retroreflectors on the antenna rim represents the geometric boresight axis of the antenna dish surface distorted by environmental loads. A means of identifying that boresight axis using SHAPES measurements is described below.

B. Main Reflector Boresight Shift Analysis

The SHAPES sources and retroreflectors are identified in Fig. 4. The three SHAPES sources, *A*, *B*, and *C*, are located on the main dish surface in the RF shadow of the quadripod at the base of the feed cone. Four retroreflectors, 1, 2, 3, and 4, are placed on the antenna rim — numbers 1 and 2 in the cross-elevation-boresight plane and numbers 3 and 4 in the elevation-boresight plane. Measurements across the dish (e.g., from point 1 to point 2 or from point 1 to point 3) are made via relay mirrors placed at rim position numbers 1 and 3.

The analytic determination of the effective structural boresight of the deformed main paraboloid is divided into three parts:

- (1) Calculate the intersection of the elevation-boresight and cross-elevation-boresight planes in the antenna rim plane.
- (2) Calculate the antenna rim plane intersection coordinates in the pointing reference plane.
- (3) Calculate the angular orientation of the effective structural boresight axis in pointing reference coordinates.

1. Calculation of the rim-plane intersection. Figure 4 illustrates the range measurements in the antenna rim plane needed to calculate the coordinates of intersection *J* relative to retro-

reflectors 1, 2, 3, and 4. The objective is to compute R_{J3} and R_{J1} given range measurements R_{12} , R_{34} , R_{13} , R_{14} , and R_{23} . The procedure is outlined below.

Calculate angles θ_1 and θ_2 by the law of cosines:

$$\theta_1 = \cos^{-1} \left[\frac{R_{12}^2 + R_{13}^2 - R_{23}^2}{2 \cdot R_{12} \cdot R_{13}} \right] \quad (1)$$

$$\theta_2 = \cos^{-1} \left[\frac{R_{13}^2 + R_{34}^2 - R_{14}^2}{2 \cdot R_{13} \cdot R_{34}} \right] \quad (2)$$

Calculate angle θ_3 :

$$\theta_3 = 180 - (\theta_1 + \theta_2) \quad (3)$$

Calculate intersection *J* locations R_{J3} and R_{J1} :

$$R_{J3} = R_{13} \cdot \frac{\sin \theta_1}{\sin \theta_3} \quad (4)$$

$$R_{J1} = R_{13} \cdot \frac{\sin \theta_2}{\sin \theta_3} \quad (5)$$

2. Calculation of intersection coordinates in the pointing reference plane. Figure 5 illustrates the placement of SHAPES sources *A*, *B*, and *C* and the projections of retroreflectors 1, 2, 3, and 4 on the pointing reference plane. Given range measurements R_{AB} , R_{BC} , R_{A1} , R_{B1} , R_{A2} , R_{B2} , R_{B3} , R_{B4} , R_{C3} , R_{C4} , R_{12} , and R_{34} , it is possible to locate the intersection *J* in the pointing reference plane in coordinates orthogonal to R_{AB} and R_{BC} in the following manner:

Calculate angles θ_4 and θ_5 :

$$\theta_4 = \cos^{-1} \left[\frac{R_{BC}^2 + R_{B3}^2 - R_{C3}^2}{2 \cdot R_{BC} \cdot R_{B3}} \right] \quad (6)$$

$$\theta_5 = \cos^{-1} \left[\frac{R_{BC}^2 + R_{B4}^2 - R_{C4}^2}{2 \cdot R_{BC} \cdot R_{B4}} \right] \quad (7)$$

Calculate the projections of retros 3 and 4 from point *B* along line *BC*:

$$K_3 = R_{B3} \cdot \cos \theta_4 \quad (8)$$

$$K_4 = R_{B4} \cdot \cos \theta_5 \quad (9)$$

Calculate the projection of the elevation component (J_Y) of intersection J relative to the vertex in pointing reference plane coordinates:

$$J_Y = K_3 + \frac{C_1}{R_{34}} (K_3 - K_4) - \frac{R_{BC}}{2} \quad (10)$$

Calculate angles θ_6 and θ_7 :

$$\theta_6 = \cos^{-1} \left[\frac{R_{AB}^2 + R_{B1}^2 - R_{A1}^2}{2 \cdot R_{AB} \cdot R_{B1}} \right] \quad (11)$$

$$\theta_7 = \cos^{-1} \left[\frac{R_{AB}^2 + R_{B2}^2 - R_{A2}^2}{2 \cdot R_{AB} \cdot R_{B2}} \right] \quad (12)$$

Calculate the projections of retros 1 and 2 from point B along line AB in the pointing reference plane:

$$K_1 = R_{B1} \cdot \cos \theta_6 \quad (13)$$

$$K_2 = R_{B2} \cdot \cos \theta_7 \quad (14)$$

Calculate the projection of the cross-elevation component (J_X) of intersection J relative to the physical vertex in pointing reference plane coordinates:

$$J_X = K_1 + \frac{C_2}{R_{12}} \cdot (K_1 - K_2) - \frac{R_{AB}}{2} \quad (15)$$

3. Calculation of the structural boresight error angles.

There are now sufficient data to determine the angular deviation of the structural boresight axis relative to the reference boresight axis. Figure 6 illustrates the reference boresight axis in a pointing reference plane, fixed coordinate frame whose origin is at the physical vertex of the main paraboloid. The elevation and cross-elevation error angle components of the main paraboloid structural boresight axis relative to the reference boresight axis are

$$\alpha_{el} = \tan^{-1} \frac{J_Y}{H} \quad (16)$$

$$\alpha_{xel} = \tan^{-1} \frac{J_X}{H} \quad (17)$$

where H = the depth of the main paraboloid from the rim plane to the surface at the vertex.

V. Subreflector Displacement Determination

A. Measurement Configuration

Figure 7 shows the baseline measurement configuration for determining the orientation of the subreflector relative to the pointing reference coordinate system. Figure 8 is a view looking into the antenna boresight axis illustrating the placement of three retroreflectors on the subreflector backup structure as viewed from three SHAPES sources located on the pointing reference plane at the base of the feed cone. Two SHAPES sources and two retroreflectors define a plane. Hence, three SHAPES sources, A , B , and C , in combination with three retroreflectors, 5, 6, and 7, define two planes with one common SHAPES-retroreflector pair. A reference coordinate frame is defined with SHAPES defining the X - Y axes and with the Z axis orthogonal to both the X and Y axes. The analysis below solves for the subreflector displacements in the pointing reference coordinate frame.

B. Subreflector Displacement Analysis

Figure 9 is an elevation view of the antenna parallel to a plane defined by two SHAPES sources, A and B , located on the pointing reference plane, and by two retroreflectors, 5 and 6, mounted on the subreflector backup structure. The interior angles θ_9 , θ_{10} , θ_{11} , and θ_{12} can be determined as follows:

$$\theta_9 = \cos^{-1} \left[\frac{R_{A6}^2 + R_{AB}^2 - R_{B6}^2}{2 \cdot R_{A6} \cdot R_{AB}} \right] \quad (18)$$

$$\theta_{10} = \cos^{-1} \left[\frac{R_{A5}^2 + R_{A6}^2 + R_{56}^2}{2 \cdot R_{A5} \cdot R_{A6}} \right] \quad (19)$$

$$\theta_{11} = \cos^{-1} \left[\frac{R_{B6}^2 + R_{AB}^2 - R_{A6}^2}{2 \cdot R_{B6} \cdot R_{AB}} \right] \quad (20)$$

$$\theta_{12} = \cos^{-1} \left[\frac{R_{A6}^2 + R_{56}^2 - R_{A5}^2}{2 \cdot R_{A6} \cdot R_{56}} \right] \quad (21)$$

The lateral subreflector displacement parallel to the line between SHAPES sources in the pointing reference plane is

$$\beta_1 = 90 - \theta_{11} \quad (22)$$

$$\Delta Y = R_{B6} \cdot \sin \beta_1 \quad (23)$$

The rotational angle of the subreflector about an axis orthogonal to the plane of Fig. 9 is

$$\beta_2 = \theta_9 - \theta_{12} \quad (24)$$

The same procedure is used to determine the translational and rotational displacements in the other plane defined by SHAPES sources *B* and *C* and retroreflectors 6 and 7.

VI. Error Sources

Both random and systematic errors affect the accuracy in the determination of antenna pointing parameters. Random errors are attributed primarily to measurement instrument resolution but are also caused by environmental effects. Scale factor variations are representative of systematic errors which affect all measurements in proportion to their magnitude. Because the scale factor of SHAPES is determined by a precision crystal oscillator, the contribution of the instrument to systematic measurement errors is insignificant. However, as with any optical time-of-flight ranging system, the measurement scale factor is affected by the speed of light in the working medium (air). The speed of light in air is inversely proportional to the index of refraction, *n*, which depends on the temperature, pressure, humidity, and carbon dioxide content, as well as on other factors. The index of refraction of air is given in [3] as

$$n = 1 + \left[\frac{(78.6 + 42.4(y - 0.0003)P)}{TZ} \right] - \left(0.00042 \cdot K \cdot es \cdot H \right) 10^{-8} \quad (25)$$

where

n = refractive index of air

y = fractional concentration of carbon dioxide by volume

P = atmospheric pressure in pascals

T = temperature in kelvins

Z = compressibility factor

H = relative humidity

K = vapor pressure enhancement factor

es = saturation vapor pressure of water vapor over water

If the values of the environmental parameters above were known exactly, the uncertainty in the determination of the refractive index of air would be estimated to be between 0.05 and 0.1 ppm due to the empirical nature of the equation. Therefore, the key environmental parameters must be measured at the antenna site to minimize time-of-flight uncertainties. On-site measurement of parameters is expected to yield a global index-of-refraction determination accuracy of 0.1 to 1.0 ppm. In addition to global uncertainties, variations due to local turbulence can add errors to individual measurements.

The random uncertainties of SHAPES have been determined by laboratory measurements to be 25 μm rms. Added to these are measurement uncertainties due to local index-of-refraction variations, which are also estimated to be approximately 25 μm rms. Since the configuration analyzed requires 14 measurements to determine the structural boresight error of the main reflector plus 7 measurements to determine the orientation of the subreflector, computer programs were needed to individually evaluate the effects of both systematic and random measurement errors on the determination of geometric pointing parameters relative to the pointing reference coordinate frame. In the random error determination programs, a measurement error increment was individually added or subtracted to each range measurement, and all possible combinations were evaluated to determine the worst case pointing parameter determination error.

VII. Error Analysis Results

Figure 10 shows the worst case main reflector boresight determination error for random SHAPES measurement resolution errors from 1×10^{-6} to 100×10^{-6} meters. A plot of the boresight determination error due to systematic measurement errors ranging from 1 ppm to 100 ppm is shown in Fig. 11. Results are plotted in Figs. 12 and 13 for subreflector lateral displacement determination errors resulting from random and systematic measurement errors. Subreflector tilt determination errors due to random and systematic measurement errors are shown in Figs. 14 and 15.

Main reflector boresight determination errors due to random measurement errors have the most significant impact on the performance of the pointing compensation configuration analyzed. The effects of expected measurement error levels on other factors affecting pointing compensation system performance are one-tenth as great or less. Based on a $\sim 35\text{-}\mu\text{m}$ -

rms overall measurement resolution (e.g., 25- μ m-rms SHAPES random error combined with 25 μ m rms of random noise due to local index-of-refraction variations), Fig. 10 shows that the main reflector structural boresight determination error is approximately 3 millidegrees. This represents the performance for the worst case combination of measurement errors and is considered to be conservative by a factor of about four.

VIII. Conclusions

This article covers work performed during fiscal year 1987. While the results are not fully conclusive, they do suggest that refinements of the technical approach have the potential to meet the 1-millidegree blind pointing accuracy required for full realization of 32-GHz (Ka-band) performance improvement.

References

- [1] M. D. Nelson, J. R. Schroeder, and E. F. Tubbs, "Optical Links in the Angle-Data Assembly of the 70-Meter Antennas," *TDA Progress Report 42-92*, vol. October–December 1987, Jet Propulsion Laboratory, Pasadena, California, pp. 154–165, February 15, 1988.
- [2] J. McLauchlan, W. Goss, and E. Tubbs, *SHAPES: A Spatial, High Accuracy, Position Encoding Sensor for Space System Control Applications*, American Astronautical Society Publication 82-032, January 20, 1983.
- [3] W. T. Estler, "High Accuracy Displacement Interferometry in Air," *Applied Optics*, vol. 24, no. 6, pp. 808–815, March 15, 1985.

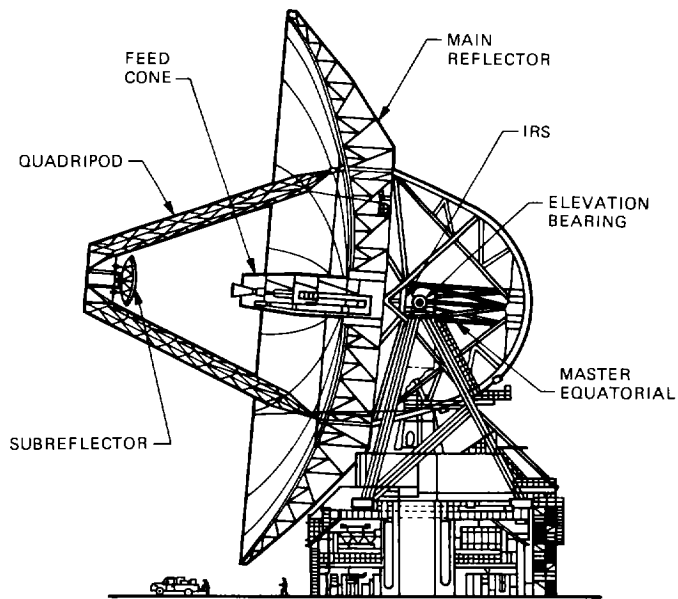


Fig. 1. The 70-meter DSN antenna

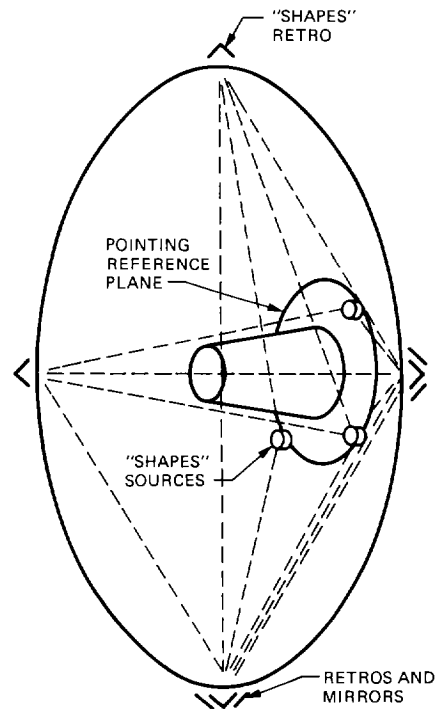


Fig. 3. Main reflector baseline measurement configuration

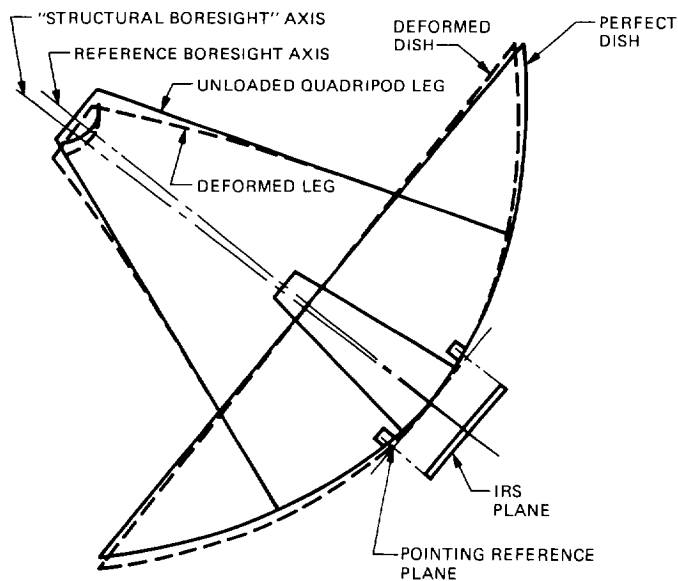


Fig. 2. Antenna deformation under environmental loads

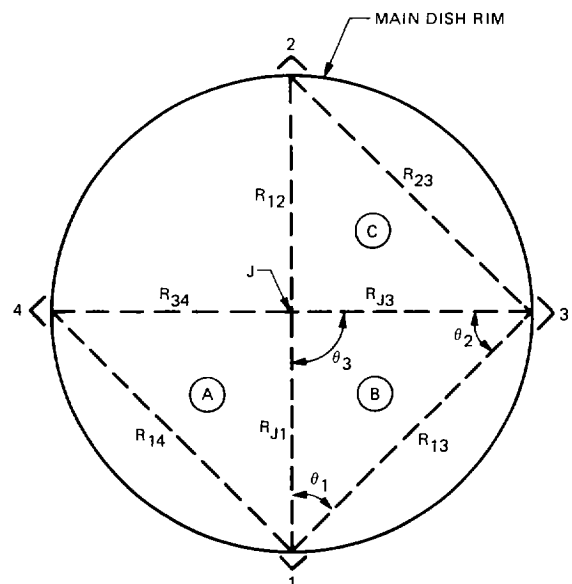


Fig. 4. Rim plane intersection (J) measurements

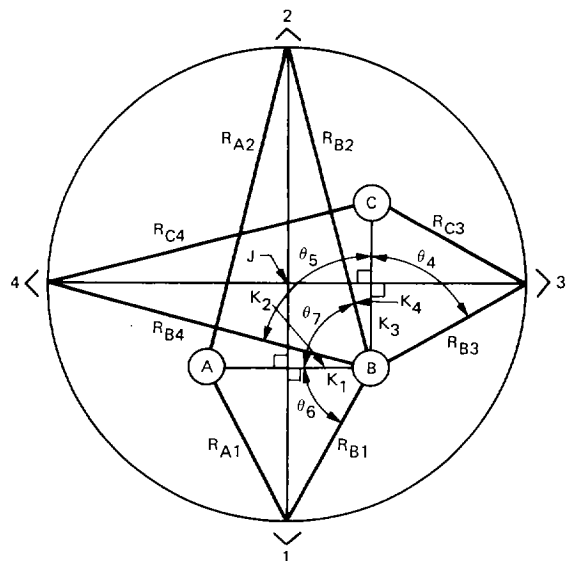


Fig. 5. Determination of J in pointing reference plane

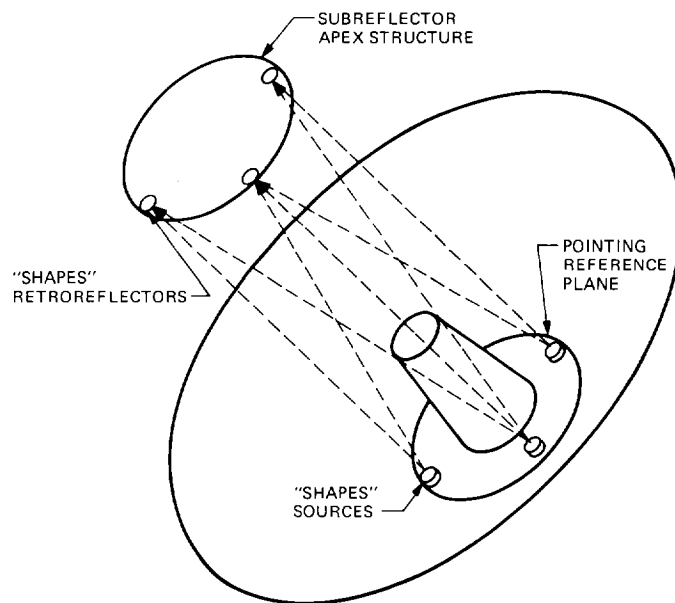


Fig. 7. Subreflector baseline measurement configuration

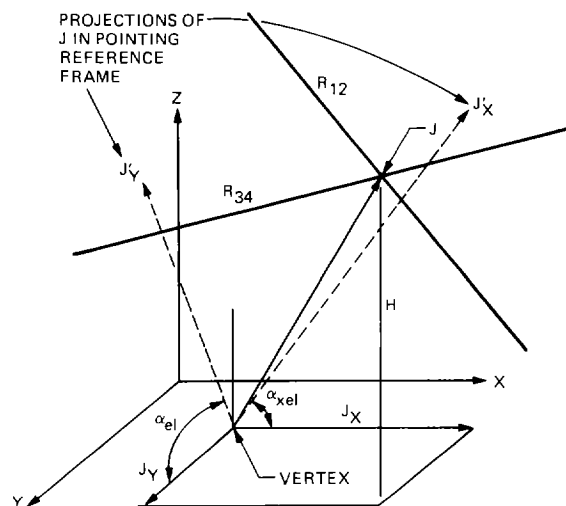


Fig. 6. Location of structural boresight axis in pointing reference coordinate frame

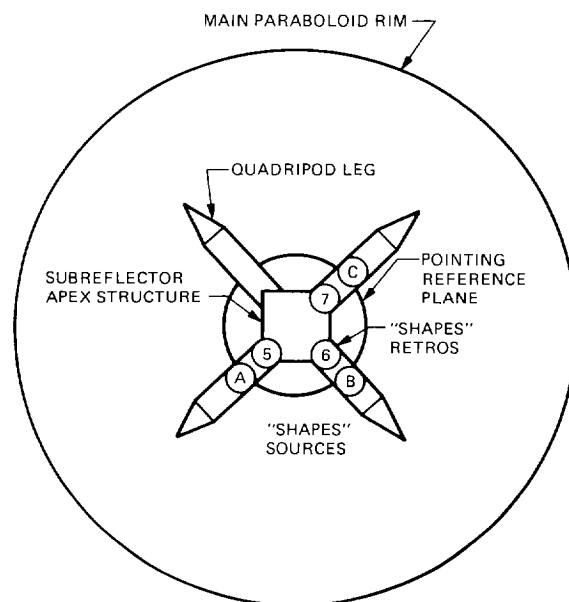


Fig. 8. Placement of SHAPES sources and retroreflectors for subreflector measurements

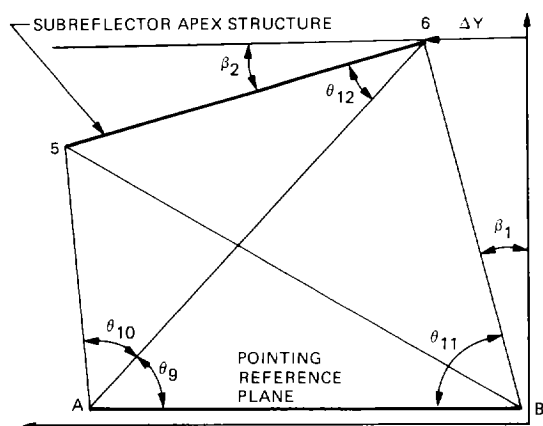


Fig. 9. Subreflector displacement measurement geometry

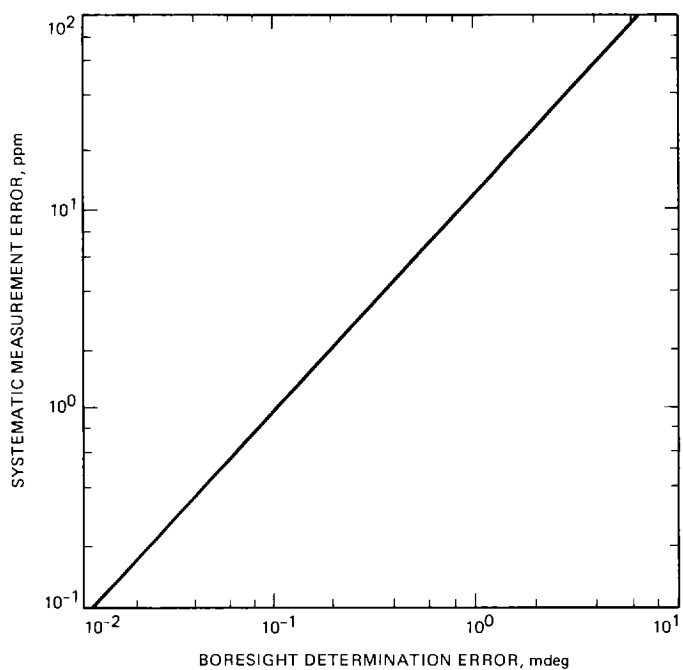


Fig. 11. Main reflector systematic boresight determination error

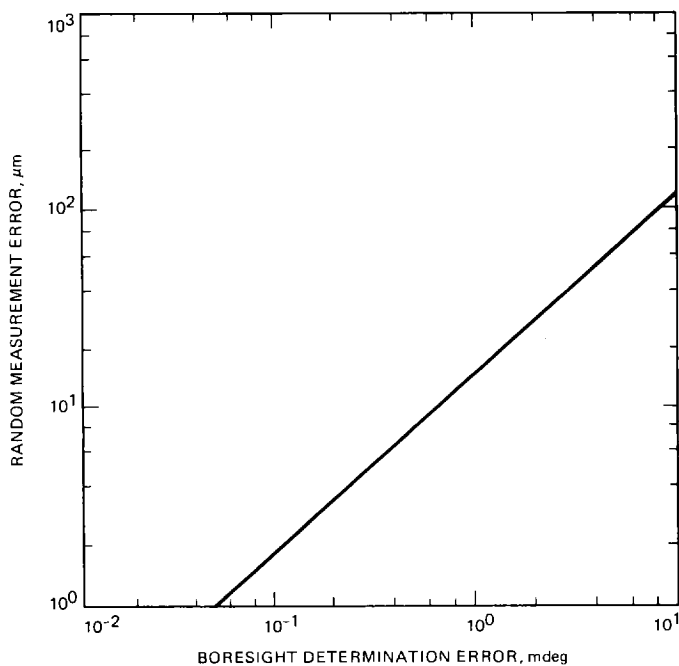


Fig. 10. Main reflector random boresight determination error

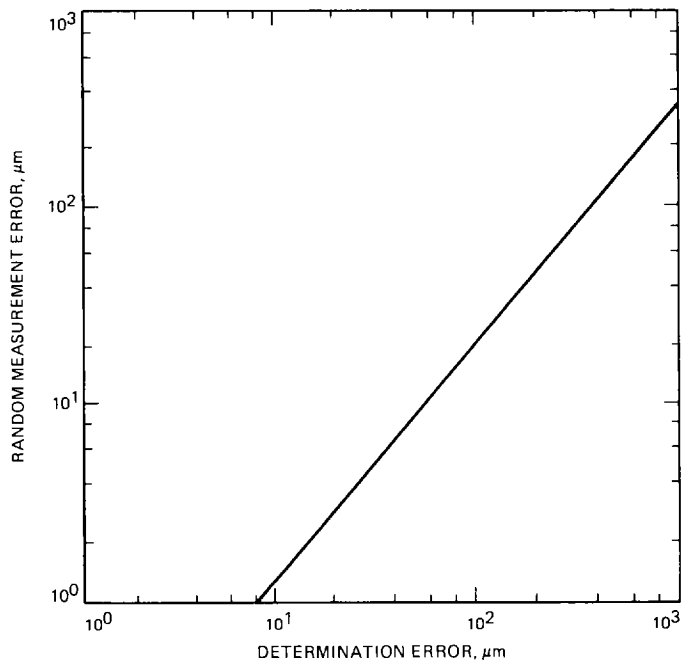


Fig. 12. Subreflector translation random determination error

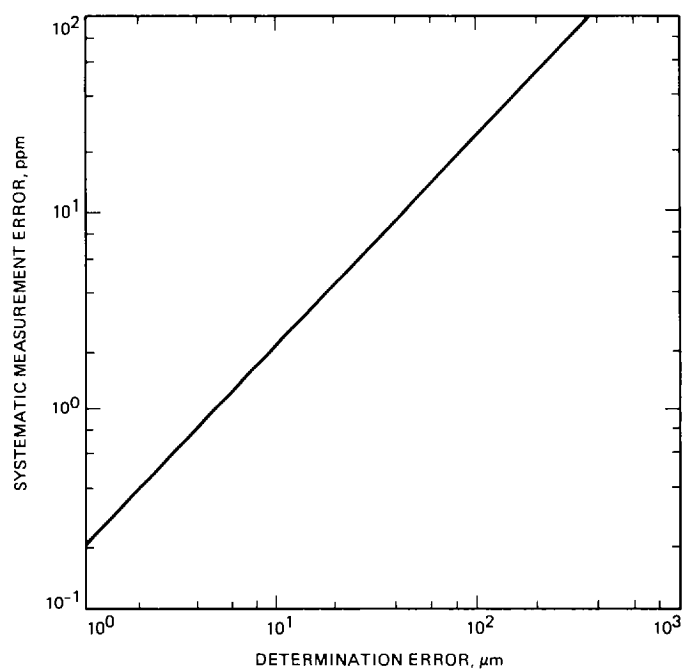


Fig. 13. Subreflector translation systematic determination error

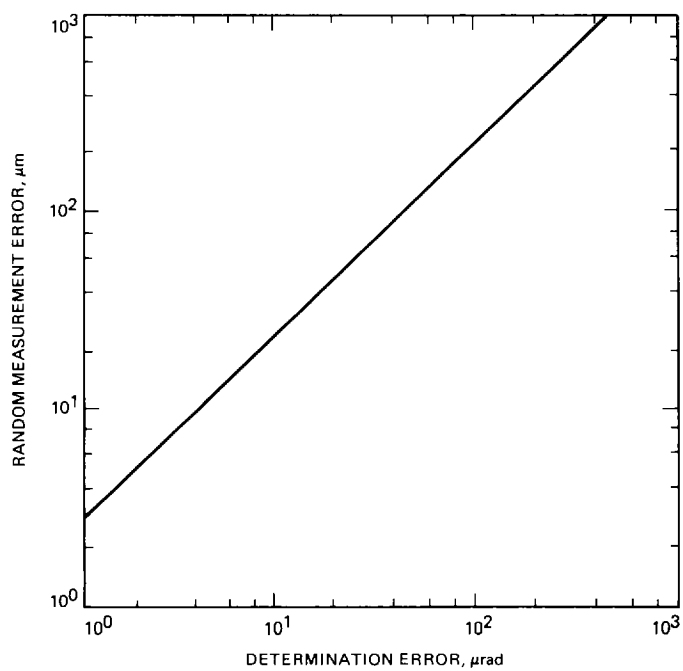


Fig. 14. Subreflector tilt random determination error

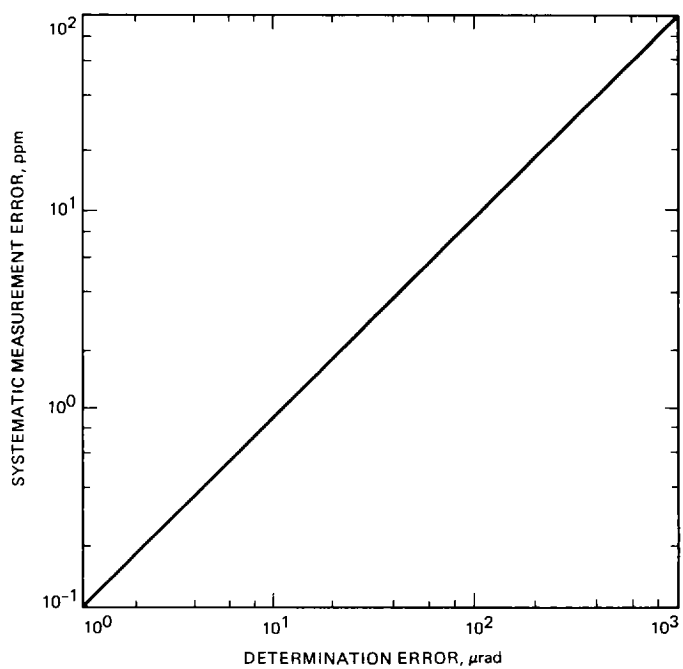


Fig. 15. Subreflector tilt systematic determination error